Journal Name

ARTICLE

High throughput fabrication of mesoporous carbon perovskite solar cells

Received 00th January 20xx,
Accepted 00th January 20xx

DOI: 10.1039/x0xx00000x

www.rsc.org/

Jenny Baker†[a], Katherine Hooper†[a], Simone Meroni[a], Adam Pockett[a], James McGettrick[a], Zhengfei Wei[a], Renan Escalante[b], Gerko Oskam[b], Matthew Carnie[a], Trystan Watson[a].

The screen printed mesoporous carbon perovskite solar cell has great potential for commercialisation due to its scalable deposition processes and use of inexpensive materials. However, each layer requires long high temperature heating steps to achieve the necessary sintering and porosity, which is very time and energy intensive for large scale production. Near infrared processing is demonstrated here to reduce the heating time of mesoporous layers within a fully printed lead halide perovskite solar cell from 2 hours to 30 seconds. A stabilised efficiency of 11% was achieved by processing in 30 seconds, identical to that of devices heated in 2 hours. For the first time the effect of residual binder in the carbon electrode on the electron lifetime and charge transfer within devices has been investigated. Furthermore cross section EDX mapping of perovskite infiltration provides a greater understanding into the processing requirements of these devices vital to enable commercialisation.

Introduction

Solution processed photovoltaic (PV) technologies such as dye sensitised solar cells (DSCs), quantum dots, perovskite and organic photovoltaics all aim to exploit the potential of lower capital and processing costs compared with silicon photovoltaics. Following the demonstration of a lead halide perovskite, $CH_3NH_3PbI_3$, as the sensitiser in a dye sensitised solar cell[1], perovskite solar cells (PSCs) as solid state devices have demonstrated the highest efficiency of all solution processed PV technologies[2][3]. The current record for a small area PSC now stands at 22.1%[4]. For commercialisation the PSC must demonstrate low cost and high stability. One of the most stable architectures is a multi-layer screen printed mesoporous stack (c-PSC) with carbon top electrode[5][6][7]. Even without encapsulation c-PSC devices are remarkably stable with lifetimes demonstrated at > 1000 hours under AM1.5 illumination[8]. Encapsulated modules have outstanding lifetimes of one year (10,000 hours, AM1.5 60°C)[9] with no loss in performance. The record PCE for the c-PSC structure is over 16%[10] and modules have been demonstrated with a PCE in excess of 10%[11][12]. The structure is versatile and different perovskites have been used to infiltrate the stack including FAPI[13] and lead-free perovskites based on bismuth[14] and copper[15]. This architecture was first demonstrated by Ku et. al[5] and involves three mesoscopic layers applied sequentially (figure 1) where an n-type mesoporous TiO_2 (m-TiO_2) layer is separated from a mesoporous carbon (m-carbon) top contact by an insulating mesoporous spacer, typically ZrO_2 (m-ZrO_2). The structure of the m-carbon top contact is particularly important to ensure optimum charge transfer between the perovskite and the carbon[16]. The three mesoporous layers are all deposited via screen printing which can ensure reproducible deposition on a large area substrate[17]. The perovskite is introduced by infiltration through the mesoporous stack and the perovskite crystal size is determined by the pores within the mesoporous structure. This avoids some of the problems of controlling perovskite crystallisation which are encountered when depositing the perovskite on a large scale rather than the more commonly used spin coating[18][19]. Infiltration on the laboratory scale is typically performed manually using a pipette but inkjet printing[20] and mechanised mesh infiltration[21] have also been demonstrated.

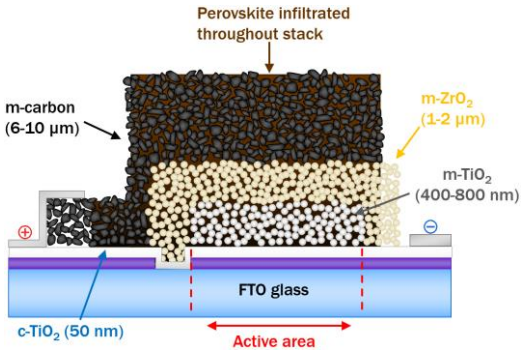

Figure 1 Schematic of a c-PSC

[a] Swansea University Bay Campus, Fabian Way, Swansea, SA1 8EN, UK.
[b] CINVESTAV, Antigua Carretera a Progreso Km 6, 97310 Mérida, Yucatan, Mexico
† These authors contributed equally to this paper
Electronic Supplementary Information (ESI) available: [planar SEM images of mesoporous layers. TGA results for m-carbon under different processing conditions, D1 cell lifetime results]. See DOI: 10.1039/x0xx00000x

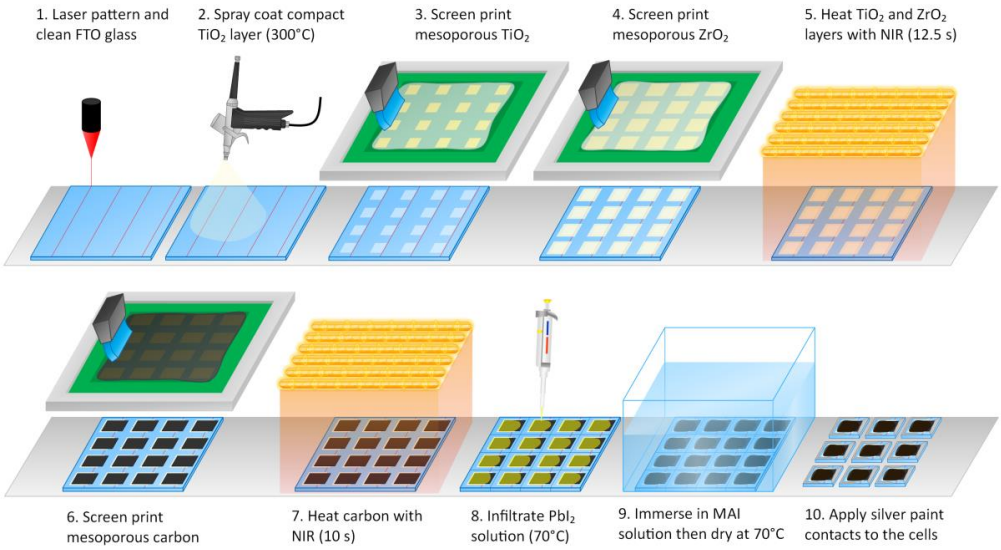

Figure 2 Schematic of a mesoporous carbon perovskite solar cell processing line.

Despite the outlined advantages the high temperature sintering of the three mesoporous layers is slow and has been highlighted as one of the barriers to commercial implementation[11,22]. Screen printing is performed at speeds of > 6 m/min but the long drying and sintering times required to induce the necessary porosity, at present over 2 hours, creates bottlenecks in the process. To enable high throughput and make the manufacture of these cells industrially viable then the heating times must be reduced. If this can be realised then an additional reduction in the large factory footprint necessitated by cumulative heating (> 400°C) steps of over 2 hours as well as a potential reduction in processing costs can be achieved.

Near infrared (NIR) technology has been used to sinter TiO_2 pastes used in dye sensitised solar cells on both glass[23] and metal substrates[24][25] for dye sensitised solar cell (DSC) applications in order to reduce manufacturing time. For the same reason NIR processing has also been used to anneal the perovskite in spin coated perovskite cells with an evaporated top contact[26]. This method involves the absorption of NIR radiation by the substrate (where the coating used is usually transparent to NIR) causing a rapid rise in temperature and a thermal gradient between the substrate surface and coating. Metal is well suited to this because it absorbs heavily in the NIR and its free carriers interact with the photons readily, transferring the heat quickly. Transparent conducting oxide (TCO) coated glass responds in a similar fashion because films such as fluorine doped tin oxide, SnO_2:F (FTO) are heavily doped degenerative semiconductors with free carriers in the conduction band.

This work examines the effect of using near infrared radiation to rapidly heat the mesoporous layers of a c-PSC in less than 12.5 seconds, enabling a line speed of 2 m/min on a small laboratory unit. The use of a typical industrial unit (1 m x 1 m) can enable a faster line speed, equivalent to 5 m/min for a processing time of 12.5 seconds. Whilst NIR heating of TiO_2[27,28] has been demonstrated previously the m-ZrO_2 and m-carbon had not been previously heated by NIR.

Whilst the morphology of the carbon particles in the m-carbon layer has been investigated previously in the c-PSC architecture the effect of binder content on device performance has not[16]. The main function of the m-carbon layer is that of a conductive top electrode, in this role residual binder does not impede cell function[29] since the carbon layer has good conductivity despite the presence of a non-conductive binder. A secondary requirement of the m-carbon layer is to enable infiltration of the perovskite after the high temperature processing steps. By understanding the parameters governing high performance in c-PSC cells the processing conditions were optimised to reduce the heating time of the mesoporous layers from over 2 hours to < 25s. This unlocks the exciting possibility of high throughput in-line processing of the m-stack, a schematic of the proposed processing line is shown in figure 2.

Methods and Materials

Cell Fabrication

TEC 7 fluorine doped tin oxide (FTO) glass substrates were etched using a Rofin Nd:YVO_4 laser (532nm) at a speed of 150 mm s^{-1}. The substrates were rinsed in isopropanol and deionised water before being O_2 plasma treated. A compact TiO_2 layer (50 nm) was deposited via spray pyrolysis at 300°C from a solution 1:9 of titanium di-isopropoxide bis(acetylacetonate) (Sigma) in isopropanol (Sigma). 30 NRD TiO_2 paste (Dyesol) 2:3 terpineol (Sigma) by weight was screen printed onto the compact TiO_2. Control cells were then sintered at 550°C for 30 minutes. ZrO_2 paste

(Solaronix) was screen printed overlapping the TiO_2 and then control cells were sintered at 400°C for 30 minutes. For the top contact carbon paste (Gwent Electronic Materials) was screen printed onto the ZrO_2 and sintered at 400°C for 30 minutes. For the NIR processed devices the c-TiO_2, m-TiO_2 and m-ZrO_2 were individually deposited (the m-TiO_2 dried at 100°C for 2 minutes) before being processed in one NIR step with an intensity of 100% at a line speed of 2 m/min using an Adphos NIR unit with 24 kW tungsten halogen emitters, schematic shown in figure S1. A conveyor, onto which the cells sit passes under the emitter with a power density of 25kw/m^2. Prior to processing a single pass is run to preheat the lamps. Following this further samples are run consecutively without further pre-heating. Adjustment of heating rate is controlled by two parameters; line speed (which corresponds to residence time) and intensity of the emitters. The m-carbon layer was then screen printed and heated at intensity of 100% at a line speed of 2.5 m/min. Onward processing of devices was the same for NIR, oven and hotplate heated devices. 1M PbI_2 (99% Sigma) was dissolved in dimethylformamide (DMF) at 70°C and 6 µl dropped onto the active area of each cell heated to 70°C. The cell was then immersed in methyl ammonium iodide solution as described previously[30].

Characterisation

A simultaneous thermal analyser (STA 6000, Perkin Elmer) was used to perform thermal gravimetric analysis on carbon, ZrO_2 and TiO_2 pastes. Tests were performed in dry air with a flow rate of 20 ml/min and heated from 30-400°C (30-550°C in the case of TiO_2) at a ramp rate of 200°C/min then held at temperature for 30 min. These temperatures are used to represent the heating regime used for each layer in the fabrication of a device. Films heated via various hot plate or NIR time/temperatures were also subjected to the same analysis so that efficacy of binder removal could be evaluated. Conductivity measurements of the m-carbon layer were performed using a four point probe and Keithley 2400 source meter. XPS & UPS analyses were carried out on a Kratos Axis Supra (Kratos Analytical, Manchester) with samples connected to ground. XPS was performed at an X-ray power of 225W using a monochromated Al source. Wide scans used a 1 eV step size and 160 eV pass energy, high resolution data with a 0.1 eV step size and 20 eV pass energy. Peaks were identified[31,32] and quantified, with carbon d-parameter analysis performed as outlined by Kaciulis[33] using CasaXPS Version 2.3.17dev6.4k with the KratosF1s sensitivity factors. UPS was carried out using the He(I) line with a pass energy of 5 eV, step size of 0.025 eV, 65 ms dwell and a 55 µm aperture to control electron flux into the analyser.

JV testing was performed using a class AAA solar simulator (Newport Oriel Sol3A) at AM1.5 with 1 sun illumination conditions calibrated against a KG5 filtered silicon reference cell (Newport Oriel 91150-KG5) and a Keithley 2400 source meter. The cells were scanned from V_{OC} to J_{SC} and vice versa at a scan rate of 0.15 V/s, 10 seconds light soaking time was applied before each measurement. Stabilised power output measurements were collected by monitoring the current with the device bias set to the maximum power point voltage as determined by the JV sweep. The active area of solar cells was defined through a metal aperture mask with an open area of 0.065 cm^2. External quantum efficiency measurements were collected using an QE X10 spectral response machine in the wavelength range between 300 nm and 850 nm. Transient photo voltage measurements were performed using a commercially available transient measurement system (Automatic Research GmbH). Measurements were performed on unmasked cells to ensure homogenous illumination. A 520 nm green laser diode was driven by a waveform generator (Keysight 33500B) to give 10 µs pulses. The laser intensity was adjusted to ensure the transient photo voltage response remained in the small perturbation regime (<10 mV amplitude). Background illumination was provided by a white LED with its intensity calibrated to generate the same device photocurrent as measured using the solar simulator. This intensity is referred to as 100% sun equivalent. Transient responses were captured by a digital storage oscilloscope (Keysight DSOX2024A), the number of sample averages being adjusted to optimise signal noise and measurement time. The device under test is assumed to be held at open-circuit by the 1 MΩ oscilloscope input. Transients were fitted to a single exponential function to extract the decay lifetime.

The cross-section morphology of the mesoporous stack was studied using a JEOL-JSM-7800F field emission scanning electron microscope (SEM) (20 kV acceleration voltage, a working distance of 10 mm and a magnification of ×15,000). Energy dispersive X-ray spectroscopy (EDX) mapping was used to deduce elemental distribution. Nitrogen adsorption measurements were taken using a Micromeritics Tristar Surface analyser, degassing time was a minimum of 4 hours at 0.02 mBar 120°C (immediately following the given heat treatment). Pore size and volume was calculated using the Barrett Joyner Halenda (BJH) method[34]. Dynamic contact angle measurements of 3µL dimethyl sulfoxide (DMSO) solvent onto a given substrate were taken every 0.064 seconds using a Nikon camera and analysed using FTA-32 software. The temperature of samples heated via NIR was estimated by filming them during exposure using an IR camera (thermoIMAGER TIM200, Micro-Epsilon). After filming, TIM Connect software was used to select the area of the sample and change the emissivity to that of the film to obtain the correct temperature.

Results and discussion

Fluorine doped tin oxide (FTO) coated glass absorbs in the NIR region peaking at 1610 nm which overlaps with the spectral output of the NIR lamp used in this work (figure 3a). The free carriers in the FTO absorb the NIR photons to rapidly reach high temperatures and transfer the heat[23]. Uncoated glass does not absorb in the NIR region so reaches lower temperatures compared to FTO glass exposed to the same NIR lamp intensity. FTO glass reaches a peak temperature of over 600°C when exposed to 100% NIR lamp intensity (25kW/m^2) whereas uncoated glass reaches only 210°C. To fabricate a perovskite solar cell using the architecture shown in figure 1 it is necessary to etch the FTO (chemically or by laser) and expose plain glass to create electrical isolation lines between

the two contacts. Initially the standard architecture FTO glass substrate was to use laser scribed lines of 1.4 mm in width. Whilst this was viable for hot plate heated cells there was an issue when using the NIR method to heat these substrates. If the temperature exceeded 500°C (necessary for the sintering of the TiO_2 particles) the substrate cracks along the isolation lines, due to thermal stress caused by the significant difference in temperature between the exposed glass and FTO. Using a finer isolation line of 0.05 mm the proportion of surrounding FTO is much greater, minimising this temperature difference and preventing cracking. This enabled uniform NIR heating to over 600°C on large substrates of FTO glass and so is used here as the standard laser scribing method for both NIR and conventional hot plate heated cells.

Figure 3a shows that the presence of a screen printed TiO_2 or ZrO_2 film (dried at 100°C and containing binder) does not affect the absorbance of FTO glass significantly because they are relatively transparent in the visible and NIR regions. The presence of the dried thin films causes interference which accounts for slight differences between them and the FTO glass only sample. Since the TiO_2 and ZrO_2 layers do not absorb, the NIR radiation will pass through them and be absorbed directly by the FTO layer. This then provides the heat to burn off the solvent/binder from the paste and sinter particles together in the case of TiO_2. Using a line speed of 2 m/min (corresponding to an NIR exposure time of 12.5 s) with 100% lamp intensity it is possible to remove all the binder (confirmed by STA) from the TiO_2 and ZrO_2 films and achieve similar appearance (figure S2-S3) to hot plate heated films. To complete devices a 6 – 10 µm carbon layer is applied on top of the TiO_2/ZrO_2 layer. SEM images (figure S4) show a composite of micron sized graphite flakes with carbon black nanoparticles to enhance conductivity.

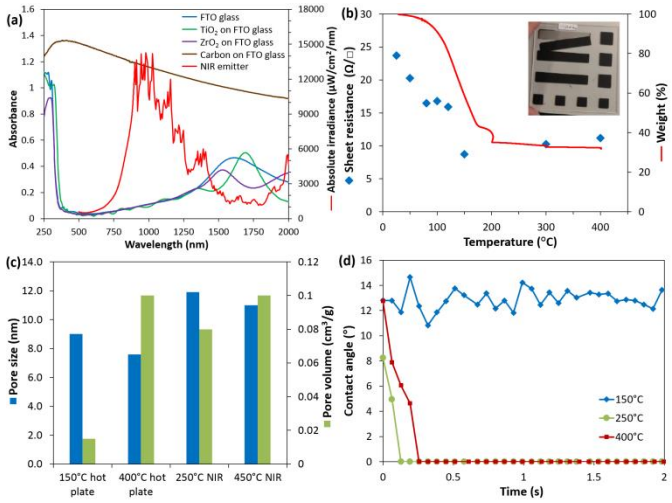

Figure 3 (a) Absorbance of FTO glass and dried films of each printed layer irradiance of the NIR emitter at 100% intensity. (b) Effect of processing temperature on sheet resistance of m-carbon. Secondary axis - TGA of carbon paste. Inset printed m-carbon on glass. (c) Effect of processing temperature on pore characteristics of m-carbon. (d) Contact angle versus time of m-carbon with different processing conditions.

The mechanism for the carbon NIR heating is different to the heating of the TiO_2/ZrO_2 films since the carbon absorbs very strongly in the visible and NIR regions (figure 3a), preventing it from reaching the FTO. Therefore the heat required to burn off the binder will be generated within the carbon layer. Although the absorption in the carbon layer is significantly higher than FTO glass alone the temperature reached with the same NIR exposure settings does not vary as greatly. For NIR processing using a line speed of 2.5 m/min (corresponding to an exposure time of 10 s) at 100% lamp intensity the carbon film reaches 450°C and FTO glass reaches 422°C (measured by IR camera). Because the carbon absorbs most of the NIR radiation before it reaches the FTO layer there is a large temperature gradient between the carbon and the FTO glass underneath which causes cracking of the cell.

To avoid the severe thermal gradient the effect of temperature and binder content of the m-carbon layer was investigated to understand the process window for heating the carbon layer. Since the carbon layer forms the top contact of the device the conductivity is critical to minimise the series resistance of the cell. On a macro scale the sheet resistance of the carbon reduces with processing temperature as the solvent is removed, shown in figure 3b. At 150°C (the manufacturer's recommended processing temperature) the sheet resistance is minimised. Further increases in processing temperature leads to a slight increase in sheet resistance in the carbon layer which is attributed to the removal of the nitrocellulose binder. With the complete removal of the binder (after heat treatment at 400°C) the carbon particles are not physically adhered to each other, or the glass substrate (see inset figure 3b). This poor adhesion to the substrate is improved when manufacturing a cell because the carbon is deposited onto a rough (Ra 50nm) ZrO_2 layer. A further increase in adhesion of the carbon to the substrate occurs during the infiltration of the perovskite.

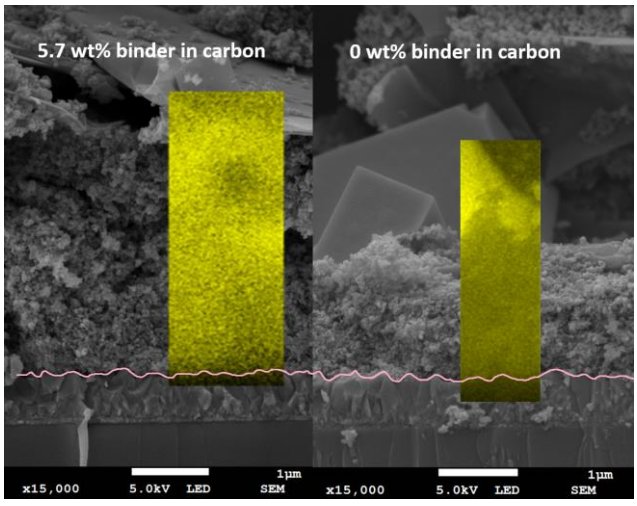

Figure 4 (a) SEM cross section of device with 5.7 wt% binder in NIR processed m-carbon layer. (b) SEM cross section of device with 0 wt% binder in NIR processed m-carbon layer. Both images: Yellow inset lead distribution through the mesoporous stack. Pink line indicates compact TiO_2 layer.

Table 1 Carbon processing conditions and corresponding binder content measured by TGA. NIR values **A-B** corresponds to A = line speed m/min and B = lamp intensity %.

Name	Heating method	Temperature (°C)	Time	Binder content (wt.%)
150°C	Hot plate	150	30 min + 30 min ramp	23
250°C	Hot plate	250	30 min + 30 min ramp	9.0
400°C	Hot plate	400	30 min + 30 min ramp	0.0
5-60 NIR	NIR	250	5 s	5.7
3-80 NIR	NIR	385	8.33 s	1.0
2.5-80 NIR	NIR	420	10 s	0.6
2.5-100 NIR	NIR	450	10 s	0.0

Once the perovskite is formed the carbon is fully adhered with the perovskite acting as a binder for the carbon particles. Nitrogen adsorption measurements were used to determine the effect of remaining binder within the m-carbon on the pore size and pore volume of the m-carbon. When the m-carbon is subject to a 150°C heat treatment the remaining binder blocks many of the pores within the m-carbon and the pore volume is only 0.01 cm^3/g, figure 3c. With such a small pore volume the PbI_2 solution will not infiltrate the carbon and the contact angle is static as shown in figure 3d. If the PbI_2 solution does not infiltrate the mesoporous structure then the TiO_2 and ZrO_2 layers remain unfilled and the device does not generate any photocurrent. By increasing the processing temperature to 250°C the pore volume increases to 0.08 cm^3/g and infiltration occurs within 0.1 seconds as shown in figure 3d. Further increases in processing temperature and pore volume do not affect the infiltration, this is confirmed by the EDX analysis of Pb distribution through the device cross section in figure 4a where Pb is seen to infiltrate through the device until the compact TiO_2 interface in both samples with 5.7 wt% binder remaining in the carbon layer and in devices where the binder is completely removed.

Having understood the process requirements to deliver a fully infiltrated device with optimum carbon conductivity devices were manufactured with NIR parameters corresponding to a processing temperature of 250°C and 5.7 wt% binder remaining in the carbon layer. However these cells had extremely poor performance exhibiting less than 2 mA/cm^2 photocurrent as shown in figure 5a and 5b. To determine the cause of the poor performance, a study with different NIR settings corresponding to different binder contents was performed. A complete list of heating settings and their corresponding binder contents, measured by STA, is given in Table 1. In order to exceed temperatures of 250°C when NIR processing the carbon layer it was necessary to use a thin steel platform (rather than the standard Teflon platform) so that the metal absorbs the NIR radiation surrounding the substrate and transfers some heat underneath the glass to help offset the temperature gradient. This enabled the carbon to reach the temperatures required to sufficiently remove all binder without cracking. Figures 5a-b show the effect of residual binder content in the NIR processed carbon layer on photovoltaic properties of the c-PSCs.

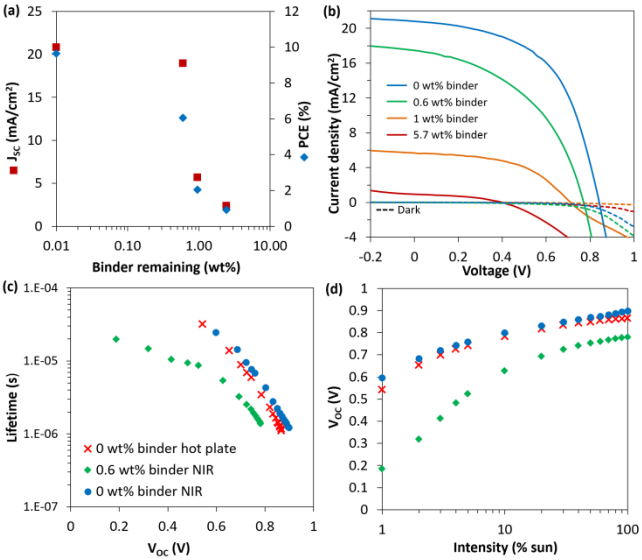

Figure 5 (a) Short circuit current (J_{SC}) and photo conversion efficiency (PCE) of solar cells manufactured with different amounts of binder (wt%) remaining in the m-carbon layer. (b) Current voltage characteristics of cells with different m-carbon processing conditions. (c) Electron lifetime versus voltage for cells with different binder content in the m-carbon layer. (d) V_{oc} versus illumination intensity for cells with different binder content in the m-carbon layer.

It can clearly be seen that unless all the binder is removed the cells do not reach optimum performance despite the good conductivity of the carbon layer and infiltration of the perovskite. Transient photo voltage (TPV) measurements, widely used to study recombination lifetimes in a range of solar cell technologies,[35–38] were used to investigate the electron lifetime in cells with residual binder. Cells with 0.6 wt% binder present in the m-carbon have electron lifetimes three times shorter than the cells with no binder at high V_{oc} values, figure 5c. This reduction in lifetime becomes more apparent at lower light intensities, which is also reflected in the drop-off in open-circuit voltage below 10% sun for cells containing 0.6 wt% binder, suggesting there is significant recombination occurring, figure 5 c and d. Poor charge injection from the perovskite into the m-carbon may lead to accumulation of holes which would promote interfacial recombination.

Table 2 – Elemental composition and physical parameters of m-carbon as a function of hot plate processing temperature.

	Surface composition (Atom %)					
Temp °C	Carbon	Oxygen	Nitrogen	D-parameter (ev)	Work function (ev)	E_f-E_{homo} (eV)
150	80.1	19.2	0.7	15.6	4.6	2.9
250	91.1	8.9	none	19.03	4.5	0
400	95.1	4.9	none	22.27	4.5	0

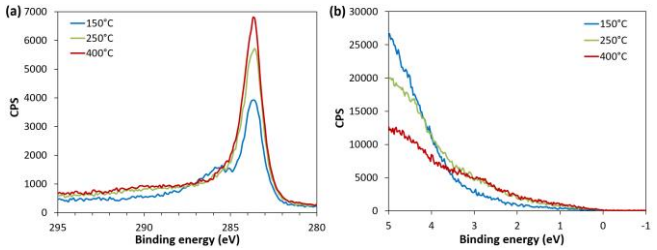

Figure 6 (a) C(1s) envelope of m-carbon with different heat treatment conditions. (b) UPS of m-carbon with different heat treatment conditions.

Cells with the binder fully removed from the carbon layer exhibit similar electron lifetimes regardless of whether the processing of the carbon layer was by hot plate or NIR, figure 5d. To further understand the role of the binder within the carbon layer the surface chemistry of the carbon was examined by XPS as a function of temperature and is summarised in Table 2. XPS analysis of the sintered carbon confirms the observations from TGA. When processed at 150°C the surface of the m-carbon shows a distinct nitrate peak at 407.8 eV (1.8 At%) and strong oxygen signals (20.9 At%) indicating that some of the residual nitrocellulose binder is still present. The oxygen is reduced markedly to 4.9 At% after 400°C processing and nitrogen eliminated entirely. With increasing processing temperature, the carbon peak continues to sharpen into a single asymmetric graphite-like structure, with the broad C-O feature at 286 eV being eliminated entirely (figure 6a). The observed increase in the d-parameter of the carbon KLL Auger structure further suggests that higher processing temperatures give the m-carbon surfaces increasing sp^2 character. To further probe this electronic change UPS was also applied to the m-carbon. Whilst the work function is fairly constant for this set of materials, it was noted that at 150°C the valence band electron density does not extend to the Fermi level.

The residual sp3 carbon from the binder has introduced a band gap such that the interface is no longer metal like (figure 6b). The poor cell performance in cells with residual binder in the carbon layer is therefore attributed to poor charge injection into the mesoporous carbon in the presences of even a small amount of non-conducting binder, despite the film having conducting properties on the macroscale. This effect is particularly important when considering the addition of polymer layers onto the carbon layer as part of an encapsulation process.

In order to confirm that NIR processing is applicable to make all layers of c-PSC, devices were manufactured using NIR for all the layers using the settings given in the experimental procedure. These cells had a total heating time for the three mesoscopic layers of 22.5 seconds, compared with the hot plate cells which had a heating time of 90 minutes at temperature (they also had ramp up and cool down times taking the total time on the hot plate to over 3 hours). To assess whether shorter heating times would be possible with

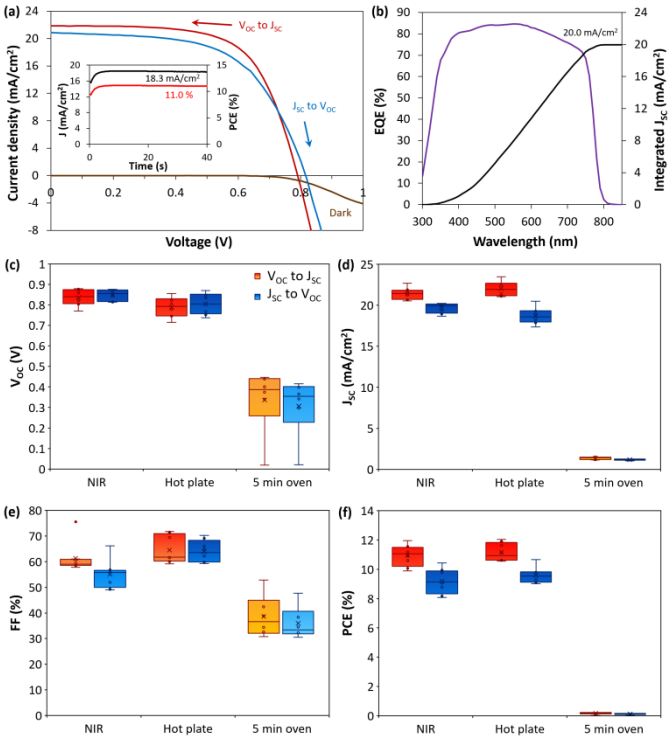

Figure 7 (a) NIR processed champion device JV curve inset: stabilised current and PCE measurement. (b) EQE and integrated current of the champion NIR device. (c-f) Box plots of current – voltage characteristics of devices manufactured with different heating conditions for the mesoporous layers. Red points indicate the V_{oc}-J_{sc} measurement, blue plots represent J_{sc} – V_{oc} measurement.

more conventional heating, devices were manufactured in an oven with each layer heated for 5 minutes at temperature. It was not possible to make devices on the hot plate without a ramping process (because the glass would crack immediately). TGA analysis determined that the binder had not been fully removed by the 5 minute high temperature treatment (table 1) and this is reflected by the extremely poor photovoltaic performance (figure 7). All the NIR devices demonstrate equivalent device performance to the hot plate heated cells figure 7c-f. The slight variation in device performance, particularly V_{oc} is due to batch to batch variation in the screen printed ZrO_2 [11], optimising an insulating layer paste is the subject of ongoing work. The champion device processed by NIR had a short circuit current of 20 mA/cm^2, verified by EQE, figure 7a-b and a stabilised PCE of 11 %. The lifetime of the NIR processed cell was equivalent to that of a hot plate processed cell with no degradation observed after 1000 hours stored in the dark, figure S5, table S1. These data also demonstrate the effect of aperture area on the cell, J_{sc} values are independent of masked area indicating a uniform cell. The fill factor drops slightly in cells with larger aperture area attributed to limitations in the conductivity of the carbon layer. Future work will concentrate on increasing the layer thickness and improving the geometry of the device in order to maintain fill factor at larger areas.

Conclusions

Near infrared heating can be used to reduce processing time and enable a line speed of 2 m/min and with all high temperature steps complete in 22.5 seconds, giving a total manufacturing time from glass to completed cell of less than 1 hour. A cell efficiency of > 11 % can be achieved by this technique equivalent to cells produced by conventional hot plate heating. With fast heating processes residual stresses caused by fast heating and cooling must be managed by designing the cell architecture for uniform heating. The conductivity of m-carbon is dependent upon residual binder content and a band gap develops when there is a residual binder present. This band gap prevents charge injection into the carbon layer from the perovskite even when the perovskite has fully infiltrated the mesoporous stack. When developing encapsulation layers the effect of insulating binders on the carbon structure must be considered to ensure optimum performance.

Acknowledgements

The authors would like to acknowledge the support provided from the Engineering and Physical Sciences Research Council (EPSRC) through the Self-assembling Perovskite Absorbers - Cells Engineered into Modules project (EP/M015254/1) and the SPECIFIC Innovation and Knowledge Centre (EP/N020863/1). The authors would also like to express their gratitude to the Welsh Government for their support of the Sêr Solar programme. A.P. and M.J.C. thank the British Council for funding, through the Newton Al-Farabi Partnership. Renán Escalante would like to thank CONACyT for a scholarship for a 6-month internship in Swansea. CONACyT is also gratefully acknowledged for funding under the Fronteras de la Ciencia programme, grant FDC-2015-110

References

[1] Kojima, A., Teshima, K., Shirai, Y., Miyasaka, T. Organometal Halide Perovskites as Visible-Light Sensitizers for Photovoltaic Cells. *Journal of the American Chemical Society* **2009**, *131* (17), 6050–6051.

[2] Lee, M. M., Teuscher, J., Miyasaka, T., Murakami, T. N., Snaith, H. J. Efficient Hybrid Solar Cells Based on Meso-Superstructured Organometal Halide Perovskites. *Science (New York, N.Y.)* **2012**, *338* (6107), 643–647.

[3] Kim, H.-S., Lee, C.-R., Im, J.-H., Lee, K.-B., Moehl, T., Marchioro, A., Moon, S.-J., Humphry-Baker, R., Yum, J.-H., Moser, J. E., Grätzel, M., Park, N.-G. Lead Iodide Perovskite Sensitized All-Solid-State Submicron Thin Film Mesoscopic Solar Cell with Efficiency Exceeding 9%. *Scientific Reports* **2012**, *2*, 1–7.

[4] Laboratory, N. R. E. Best research cell efficiencies https://www.nrel.gov/pv/assets/images/efficiency-chart.png (accessed Apr 10, 2017).

[5] Mei, A., Li, X., Liu, L., Ku, Z., Liu, T., Rong, Y., Xu, M., Hu, M., Chen, J., Yang, Y., Grätzel, M., Han, H. A Hole-Conductor–free, Fully Printable Mesoscopic Perovskite Solar Cell with High Stability. *Science* **2014**, *345* (6194), 295–298.

[6] Ku, Z., Rong, Y., Xu, M., Liu, T., Han, H. Full Printable Processed Mesoscopic $CH_3NH_3PbI_3/TiO_2$ Heterojunction Solar Cells with Carbon Counter Electrode. *Scientific reports* **2013**, *3*, 3132.

[7] Cai, M., Wu, Y., Chen, H., Yang, X., Qiang, Y., Han, L. Cost-Performance Analysis of Perovskite Solar Modules. *Advanced Science* **2016**.

[8] Li, X., Dar, M. I., Yi, C., Luo, J., Tschumi, M., Zakeeruddin, S. M., Nazeeruddin, M. K., Han, H., Grätzel, M. Improved Performance and Stability of Perovskite Solar Cells by Crystal Crosslinking with Alkylphosphonic Acid Ï-Ammonium Chlorides. *Nature Chemistry* **2015**, *7* (9), 703–711.

[9] Grancini, G., Zimmermann, I., Mosconi, E., Martineau, D., Narbey, S., Oswald, F., De Angelis, F., Graetzel, M., Nazeeruddin, M. K. One-Year Stable Perovskite Solar Cells by 2D / 3D Interface Engineering. *Nature Chemistry* **2017**, No. 14, 1–8.

[10] Zhang, H., Wang, H., Williams, S. T., Xiong, D., Zhang, W., Chueh, C.-C., Chen, W., Jen, A. K.-Y. $SrCl_2$ Derived Perovskite Facilitating a High Efficiency of 16% in Hole-Conductor-Free Fully Printable Mesoscopic Perovskite Solar Cells. *Advanced Materials* **2017**, 1606608.

[11] Hu, Y., Si, S., Mei, A., Rong, Y., Liu, H., Li, X., Han, H. Stable Large-Area (10×10 cm^2) Printable Mesoscopic Perovskite Module Exceeding 10% Efficiency. *Solar RRL* **2017**, 1600019.

[12] Priyadarshi, A., Haur, L. J., Murray, P., Fu, D., Kulkarni, S., Xing, G., Sum, T. C., Mathews, N., Mhaisalkar, S. G. Environmental Science. *Energy & Environmental Science* **2016**, *9*, 3687–3692.

[13] Hu, M., Liu, L., Mei, A., Yang, Y., Liu, T., Han, H. Efficient Hole-Conductor-Free, Fully Printable Mesoscopic Perovskite Solar Cells with a Broad Light Harvester $NH_2CH{=}NH_2PbI_3$. *Journal of Materials Chemistry A* **2014**, *2* (40), 17115–17121.

[14] Li, T., Hu, Y., Morrison, C., Wu, W., Han, H., Robertson, N. Lead-Free Pseudo-Three-Dimensional Organic-Inorganic Iodobismuthates for Photovoltaic Applications. *Sustainable Energy Fuels* **2017**, *1*, 308–316.

[15] Li, X., Zhong, X., Hu, Y., Li, B., Sheng, Y., Zhang, Y., Weng, C., Feng, M., Han, H., Wang, J. Organic-Inorganic Copper(II)-Based Material: A Low-Toxic, Highly Stable Light Absorber for Photovoltaic Application. *The Journal of Physical Chemistry Letters* **2017**, No. 8, 1804–1809.

[16] Liu, T., Liu, L., Hu, M., Yang, Y., Zhang, L., Mei, A., Han, H. Critical Parameters in TiO_2/ZrO_2/Carbon-Based Mesoscopic Perovskite Solar Cell. *Journal of Power Sources* **2015**, *293* (October), 533–538.

[17] Jewell, E., Philip, B., Greenwood, P., Weirmann, C. Material and Process Optimization Screen Printing Carbon Graphite Pastes for Mass Production of Heating Elements. *Journal of Manufacturing Processes* **2015**, *22*, 185–191.

[18] Baker, J. A., Mouhamad, Y., Hooper, K. E. A., Burkitt, D., Geoghegan, M., Watson, T. M. From Spin Coating to Roll-to-Roll : Investigating the Challenge of Upscaling Lead Halide Perovskite Solar Cells. *IET Renewable Power Generation* **2017**, *11* (5), 546 – 549.

[19] Cotella, G., Baker, J., DeRossi, F., Pleydell-Pearce, C., Carnie, M., Watson, T. One-Step Deposition by Slot-Die Coating of Mixed Lead Halide Perovskite for Photovoltaic Applications. *Solar Energy Materials and Solar Cells* **2017**,

159, 362–369.

[20] Hashmi, S. G., Martineau, D., Li, X., Ozkan, M., Tiihonen, A., Dar, M. I., Sarikka, T., Zakeeruddin, S. M., Paltakari, J., Lund, P. D., Grätzel, M. Air Processed Inkjet Infiltrated Carbon Based Printed Perovskite Solar Cells with High Stability and Reproducibility. *Advanced Materials Technologies* **2016**, 1600183.

[21] Meroni, S., Mouhamad, Y., De Rossi, F., Pockett, A., Baker, J., Escalante, R., Searle, J., Carnie, M., Jewell, E., Oskam, G., Watson, T. Large Area Homogeneous Deposition of Perovskite in Fully-Printable Perovskite Solar Cells. *Science and Technology of Advanced Materials* **2017**, Focus Issue, under review.

[22] Chen, H., Yang, S. Carbon-Based Perovskite Solar Cells without Hole Transport Materials: The Front Runner to the Market? *Advanced Materials* **2017**, No. February.

[23] Hooper, K., Charbonneau, C., Carnie, M., Watson, T. Near Infrared Radiation as a Rapid Heating Technique for TiO_2 Films on Glass Mounted Dye-Sensitized Solar Cells. *International Journal of Photoenergy* **2014**, *953623* (February).

[24] Holliman, P. J., Davies, M. L., Connell, A., Vaca Velasco, B., Watson, T. M. Ultra-Fast Dye Sensitisation and Co-Sensitisation for Dye Sensitized Solar Cells. *Chemical communications (Cambridge, England)* **2010**, *46* (38), 7256–7258.

[25] Carnie, M. J. The Characterization and Prevention of UV Photodegradation of Dye-Sensitized Solar Cells. **2011**.

[26] Troughton, J., Charbonnaeu, C., Carnie, M. J., Davies, M. L., Worsley, D. A., Watson, T. M. Rapid Processing of Perovskite Solar Cells in under 2.5 Seconds. *J. Mater. Chem. A* **2015**, 9123–9127.

[27] Charbonneau, C., Cameron, P. J., Pockett, A., Lewis, A., Troughton, J. R., Jewell, E., Worsley, D. A., Watson, T. M. Solution Processing of TiO_2 Compact Layers for 3rd Generation Photovoltaics. *Ceramics International* **2016**, *42*, 11989–11997.

[28] Carnie, M. J., Charbonneau, C., Barnes, P. R. F., Davies, M. L., Mabbett, I., Watson, T. M., O'Regan, B. C., Worsley, D. a. Ultra-Fast Sintered TiO_2 Films in Dye-Sensitized Solar Cells: Phase Variation, Electron Transport and Recombination. *J. Mater. Chem. A* **2013**, *1* (6), 2225–2230.

[29] Wei, Z., Zheng, X., Chen, H., Long, X., Wang, Z., Yang, S. A Multifunctional C+epoxy/Ag-Paint Cathode Enables Efficient and Stable Operation of Perovskite Solar Cells in Watery Environments. *J. Mater. Chem. A* **2015**.

[30] Hooper, K. E. A., Lee, H. K. H., Newman, M. J., Meroni, S., Baker, J., Watson, T. M., Tsoi, W. C. Probing the Degradation and Homogeneity of Embedded Perovskite Semiconducting Layers in Photovoltaic Devices by Raman Spectroscopy. *Phys. Chem. Chem. Phys.* **2017**, *131*, 6050–6051.

[31] NIST X-ray Photoelectron Spectroscopy Database, Version 4.1 http://srdata.nist.gov/xps/ (accessed May 31, 2017).

[32] Moulder, J. F., Stickle, W. F., Sobol, P. E., Bomben, K. D. *Handbook of X-Ray Photoelectron Spectroscopy.*; Physical Electronics: Minnesota, 1985.

[33] Kaciulis, S. Spectroscopy of Carbon: From Diamond to Nitride Films. *Surf. Interface Anal.* **2012**, *44*, 1155–1161.

[34] Barrett, E. P., Joyner, L. G., Halenda, P. P. The Determination of Pore Volume and Area Distributions in Porous Substances. I. Computations from Nitrogen Isotherms. *Journal of the American Chemical Society* **1951**, *73* (1), 373–380.

[35] Hawks, S. A., Deledalle, F., Yao, J., Rebois, D. G., Li, G., Nelson, J., Yang, Y., Kirchartz, T., Durrant, J. R. Relating Recombination, Density of States, and Device Performance in an Efficient Polymer:Fullerene Organic Solar Cell Blend. *Advanced Energy Materials* **2013**, *3* (9), 1201–1209.

[36] O'Regan, B. C., Barnes, P. R. F., Li, X., Law, C., Palomares, E., Marin-Beloqui, J. M. Optoelectronic Studies of Methylammonium Lead Iodide Perovskite Solar Cells with Mesoporous TiO2: Separation of Electronic and Chemical Charge Storage, Understanding Two Recombination Lifetimes, and the Evolution of Band Offsets during J–V Hysteresis. *Journal of the American Chemical Society* **2015**, *137* (15), 5087–5099.

[37] Barnes, P. R. F., Miettunen, K., Li, X., Anderson, A. Y., Bessho, T., Gratzel, M., O'Regan, B. C. Interpretation of Optoelectronic Transient and Charge Extraction Measurements in Dye-Sensitized Solar Cells. *Advanced Materials* **2013**, *25* (13), 1881–1922.

[38] Pockett, A., Carnie, M. J. Ionic Influences on Recombination in Perovskite Solar Cells. *ACS Energy Letters* **2017**, *Just accepted*.

